Space Sci Rev (2009) 147: 89–110
DOI 10.1007/s11214-009-9577-7

Interplanetary Coronal Mass Ejections Observed in the Heliosphere: 3. Physical Implications

Timothy A. Howard · S. James Tappin

Received: 6 March 2009 / Accepted: 22 September 2009 / Published online: 28 October 2009

Abstract We conclude the heliospheric image series with this third and final instalment, where we consider the physical implications of our reconstruction of interplanetary coronal mass ejections from heliospheric imagers. In Paper 1 a review of the theoretical framework for the appearance of ICMEs in the heliosphere was presented and in Paper 2 a model was developed that extracted the three-dimensional structure and kinematics of interplanetary coronal mass ejections directly from SMEI images. Here we extend the model to include STEREO Heliospheric Imager data and reproduce the three-dimensional structure and kinematic evolution of a single Earth-directed interplanetary coronal mass ejection that was observed in November 2007. These measurements were made with each spacecraft independently using leading edge measurements obtained from each instrument. We found that when data from the three instruments was treated as a single collective, we were able to reproduce an estimate of the ICME structure and trajectory. There were some disparities between the modelled ICME and the *in situ* data, and we interpret this as a combination of a slightly more than spherically curved ICME structure and a corotating interaction region brought about by the creation of a coronal hole from the CME eruption. This is the first time evidence for such a structure has been presented and we believe that it is likely that many ICMEs are of this nature.

Keywords Coronal mass ejections · Solar-terrestrial relations · Interplanetary medium · Corotating interaction regions

1 Introduction

Coronal mass ejections (CMEs) and their interplanetary counterparts (ICMEs) are large eruptions of magnetic field and solar plasma, with a likely source in the lower solar corona.

T.A. Howard (✉) · S.J. Tappin
Air Force Research Laboratory, National Solar Observatory, Sunspot, NM 88349, USA
e-mail: howard@boulder.swri.edu

T.A. Howard
Now at: Department of Space Studies, Southwest Research Institute, Boulder, CO 80302, USA

They are the mechanism by which the Sun removes large amounts of energy and magnetic helicity and their occasional impact with the Earth may result in large space weather effects. Their sizes may span several tens of degrees of heliospheric latitude, their masses may exceed 10^{13} kg and early in their evolution they may achieve speeds greater than 3000 km/s.

Until recently, the study of the three-dimensional (3-D) structure and evolution of CMEs has been limited primarily to modelling efforts and *in situ* data measurements (e.g. Lepping et al. 1990; Chen 1996; Xie et al. 2004). Using CME images alone, 3-D measurements were not possible because of sky-plane projection effects and only estimates of 3-D structure could be made using known associations of CMEs with solar surface phenomena such as flares (e.g. Howard et al. 2008b), prominences/filaments (e.g. Howard et al. 2007) and post-eruptive arcades (Tripathi et al. 2004). The first attempt at producing 3-D structures comparing CMEs and ICMEs using data alone was published in 2007 (Howard et al. 2007), but was based on solar surface associations. A further attempt at 3-D reconstruction using coronagraph data alone was performed by Howard and Tappin (2008).

Existing models that are able to produce simulated images of ICMEs couple two separate physical problems:

1. The physics responsible for the appearance of the ICME. This is a combination of the Thomson scattering physics responsible for the observed intensity and polarisation and of the relative geometry of the large structure, which includes integrated lines of sight and the overall 3-D structure. The theory behind this is outlined in Howard and Tappin (2009).
2. The physics responsible for the evolution of the ICME. This may include, for example, a possible Lorentz driving force (e.g. Chen 1996), aerodynamic drag effects (e.g. Cargill 2004; Tappin 2006) or dynamic interaction with the surrounding solar wind (e.g. Hakamada and Akasofu 1982; Fry et al. 2001).

With such models, an assumption is made about the physical evolution mechanism which is then coupled with the physics responsible for the appearance of the ICME to produce an image sequence relative to any arbitrary observer such as at the Earth or normal to the ecliptic plane. Boundary conditions are then modified in an often *ad hoc* fashion in order to match the modelled images with those observed in the data. The coupling of these two problems, we believe, is the primary reason for why existing ICME models are inadequate at predicting ICME evolution, particularly the timing of their arrival at 1 AU.

In the current series of papers we attempt to decouple the two problems by extracting the 3-D structure and kinematics from the ICME images without considering the physics responsible for the evolution of the ICME. In the first part of the series (Howard and Tappin 2009, hereafter referred to as Paper 1), a review of the theory responsible for the appearance of ICMEs was presented. This built up the picture of the ICME from the Thomson scattering physics from a single election, to an integrated line of sight, and finally with a consideration of the ICME as a large 3-D structure. The variation of the leading edge of this structure relative to a fixed observer was considered as the ICME expanded through the heliosphere. This theoretical consideration laid the foundations for the development of the model now known as the TH Model, which was developed and discussed in the second part of the series (Tappin and Howard 2009, hereafter referred to as Paper 2). The TH Model begins with a sequence of leading edge measurements of ICMEs observed with heliospheric imagers and compares them with a hypercube of simulated ICME leading edges. The result is a series of a matching parameter combination describing the 3-D structure and kinematic evolution of the ICME. Hence using leading edge measurements from heliospheric image data alone, the TH Model reproduces the 3-D structure of the ICME, and identifies its direction of propagation,

and distance, speed and acceleration properties. The model was tested using two events observed by the Solar Mass Ejection Imager in 2004 which were compared with associated CME coronagraph data and *in situ* near-Earth spacecraft data. The Model identified both the timing of the associated LASCO CME and the arrival time at 1 AU with remarkable precision.

The present paper concludes the heliospheric image series with a consideration of the physical implications of the TH Model. We consider a single event observed in November 2007 and extend the Model to accommodate for the Heliospheric Imagers on board the STEREO spacecraft. This modification treats measurements from the three spacecraft as a single collective and the 3-D structure and kinematic properties for the same event are extracted. An accurate reconstruction of this event was produced by first using the TH model 3-D reconstruction as a starting point, and the structure was then refined using the *in situ* data as a guide. We find that the best description of this model is a combination of a "standard" ICME coupled with a corotating interaction region structure extending from the western flank. To match the *in situ* data accurately it was required that the ICME component be slightly more curved than the spherical shell used in the Model.

2 Data

The selected event was detected by a variety of imaging and *in situ* instruments, and those which were used in the present study are listed below.

1. The Large Angle Spectroscopic COronagraph (LASCO) imaging instrument on board SOHO (Brueckner et al. 1995). LASCO currently has two functioning coronagraphs, C2 which has a field of view (FOV) of 1.5–6 $R_\odot$ and a cadence of around 30 minutes, and C3 with a FOV of 3.7–30 $R_\odot$ and cadence of around 50 minutes. LASCO has observed well over 10^4 CMEs over its 14 year lifetime and its observations have been well documented (e.g. St. Cyr et al. 2000; Yashiro et al. 2004).
2. The COR coronagraphs on board the twin STEREO spacecraft (Kaiser et al. 2008). These spacecraft orbit the Sun with a similar orbit to that of the Earth, except that one spacecraft (STEREO-A) leads while the other (STEREO-B) lags. The angular separation between each spacecraft and the Sun-Earth line grows by ∼22.5° per year, so by the time of our selected event they were each ∼20° away from the Earth (and ∼40° from each other). There are two coronagraphs aboard each spacecraft, COR1 (Thompson and Reginald 2008) which has a FOV of 1.1–3.0 $R_\odot$ and cadence of 5 minutes, and COR2 (e.g. Howard et al. 2008a) with a FOV of 2–15 $R_\odot$ and cadence 30 minutes. CME observations using the STEREO CORs have been reported by Mierla et al. (2008) and Howard and Tappin (2008). The present event was only observed with COR2.
3. The Solar Mass Ejection Imager (SMEI) instrument on board Coriolis (Eyles et al. 2003; Jackson et al. 2004). SMEI images the entire sky in white light beyond 20° elongation, and each all-sky image is acquired during the spacecraft's 102 minute polar orbit. Reports of ICME observations using SMEI include Tappin et al. (2004), Howard et al. (2006) and Webb et al. (2006).
4. The Heliospheric Imager (HI) imaging instruments on board STEREO (Eyles et al. 2009). There are two HI instruments aboard each spacecraft, HI-1 has a FOV of around 4.4–20.4° elongation and cadence of 40 minutes while HI-2 has a FOV around 18.7–88.7° elongation and cadence of 120 minutes. The HI cameras are not Sun-centred, but rather are centred to allow a continuous FOV from the Sun to near 90° elongation, by combining the HIs and CORs. The HIs have a circular FOV, and as such do not observe

the high-latitude regions of the heliosphere. They also effectively only observe the Earthward side of the Sun. Observations of ICMEs observed using the HIs include Harrison et al. (2008) and Webb et al. (2009).

5. The MAG magnetometer (Smith et al. 1998) and Solar Wind Electron Proton Alpha Monitor (SWEPAM) (McComas et al. 1998) particle detector on board the *in situ* ACE spacecraft. Reports using measurements of ICMEs using these instruments include Lynch et al. (2003), Dal Lago et al. (2004) and Reinard (2008).
6. The MAG magnetometer (Acuña et al. 2008), and Solar Wind Electron Analyzer (SWEA) particle detector (Sauvaud et al. 2008), part of the *in situ* IMPACT and PLASTIC instrument suite (Acuña et al. 2008; Galvin et al. 2008) aboard STEREO. The magnetometer provides triaxial measurements with an intrinsic sample rate of 32 samples/s, sensitive to 0.015 nT. SWEA measures the distribution function of the solar wind core, halo and strahl electrons from 1 to around 3000 eV. Measurements of ICMEs using IMPACT have been presented by Marubashi et al. (2008) and Möstl et al. (2008).

Along with direct observation, other phenomena associated with the CME/ICME were also observed. These include:

1. Associated solar "surface" activity, observed by the Extreme-ultraviolet Imaging Telescope (EIT) (Delaboudinière et al. 1995). EIT obtains whole-disk images of the Sun roughly every 12 minutes. The wavelength most frequently observed by this instrument is the 195 Å Fe XII line, which is common at temperatures of around 1.5×10^6 K.
2. Increased geomagnetic activity recorded by the ground-based magnetometers used to determine the 3-hourly K_p and the hourly Dst indices. Disturbed geomagnetic activity is indicated roughly by a K_p value >4 and Dst <-30 nT.

Other solar observatory data were also inspected, such as the GOES X-ray monitors and the ground-based Hα telescope network, but these revealed no substantial activity on the solar surface around the launch time of this event.

3 The Event

The event was observed by each of the above instruments at various times during its passage from 0 to 1 AU and beyond, during the time period from 15–20 November 2007. The associated geomagnetic storm occurred 20–21 November.

3.1 Coronagraph and HI-1 Observations

The CME was first observed by COR2-B on 15 November around 18:10 UT, then by COR2-A around 18:40 UT, and in LASCO C2 around 18:50 UT. It was detected as a faint, slow-moving CME predominantly in the north-northwest quadrant of the sky in LASCO, northwest in COR2-A and west in COR2-B. It appears as a partial halo CME (i.e. a CME with a component directed along the Sun-observer line) in all three instruments, but it is most easily observed in COR2-B. Sky-plane-projected speeds for the CME are roughly 150 km/s from LASCO, 140 km/s from COR2-A and 155 km/s from COR2-B, but an acceleration is observed by all three (refer to Fig. 7b). A separate (but possibly related) narrow structure extends to the east in LASCO and COR2-A, but it does not appear in COR2-B. Figure 1 shows images of the CME from each coronagraph and the inner HI camera (HI-1), with panel (a) showing LASCO C2, (c) showing COR2-A and (d) showing COR2-B. These have been selected to represent the appearance of the CME at the same time in each coronagraph

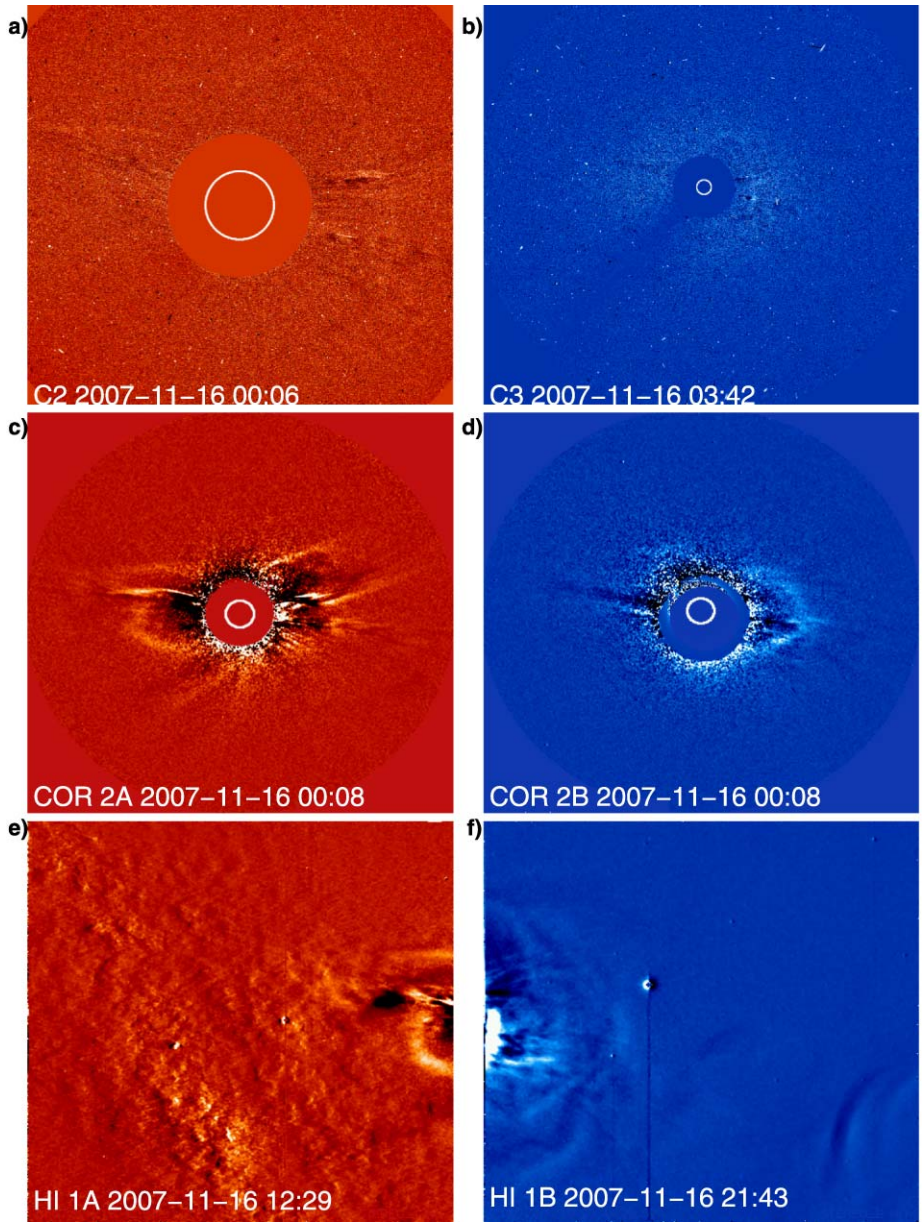

Fig. 1 Coronagraph and HI-1 images for the event. Each image was obtained on 16 November. (**a**) LASCO C2, (**c**) COR2-A and (**d**) COR2-B images around 00:06 UT, (**b**) LASCO C3 image at 03:42 UT, (**e**) HI-1A image at 12:24 UT, and (**f**) HI-1B image at 21:44 UT. The solar disk is indicated by the *white circle* in panels (**a**)–(**d**) and the *filled circle* at the centre represents the coronagraph occulting disk. For the HI images the Sun is not in the images, but rather is located to the *right* of panel (**e**) and to the *left* of panel (**f**). For each image the instrument, date and time are labelled

(16 November around 00:06 UT). Further from the Sun projection affects play a role in the timing of the transit of the CME across the relative FOV of each camera. So Figs. 1b, 1e and 1f show LASCO C3, HI-1A and HI-1B images at different times (03:42, 12:24 and 21:44 UT respectively), although each on 16 November.

Two other significant CMEs were observed in coronagraphs around the time of this event, both directed towards the southwest with no Earth-directed component. The first was observed the day before the present event, on 14 November while the second the day after on 16 November. These have been studied in detail by Howard and Tappin (2008) and the earlier event appears in the HI-2B image toward the bottom right in Fig. 1f. It is possible that a common magnetic structure may be partially responsible for all three events, although for the present event to be Earth-directed there would need to be a contribution from the western hemisphere of the Sun (relative to the Earth), a component not believed to be part of the other two events.

3.2 SMEI and HI-2 Observations

Further into the heliosphere, the ICME counterpart was observed by SMEI and both HI-2 instruments. Images from each are shown in Fig. 2. It should be noted that for the purposes of the TH Model only the events observed in the heliospheric images are relevant. While helpful for independent comparison purposes, the Model does not use coronagraph data directly.

The event first appeared in Camera 2 of SMEI on 19 November in the image from 01:44 to 03:26 UT. It was brightest in the south-southeast quadrant and later extended toward the southwest. It was last observed leaving the Camera 2 FOV in the southwest around 12:00 UT on 20 November. At this time SMEI became saturated with aurora and particle precipitation most likely caused by the geomagnetic storm. In other words, SMEI observed the transient until it impacted the Earth, after which it was blinded by the effects of increased geomagnetic activity. Figures 2a show two selected zenithal equidistant ("fisheye") images of the ICME observed in SMEI.

It was first observed in HI-2A early on 19 November immediately after a 24-hour data gap. The ICME was visible as a faint band moving through the northern (upper) region of the outer (left) part of the FOV. It was observed until it moved beyond the FOV by 12:09 UT on 20 November. At larger elongations there appeared to be two bands present, both of which appeared to become convex-inward (i.e. with their peaks pointing towards the Sun) beyond elongations around 50°. It is unclear whether these are due to two separate structures or whether these are the effects of projection or the optics of the instrument. Figures 2b show two selected HI-2A images of the ICME.

Figures 2c show three images of the event as observed by HI-2B. Here the ICME appeared at 18 November around 12:09 UT following the previous brighter "limb" CME reported by Howard and Tappin (2008). At smaller elongations (towards the left of the FOV) the event was visible throughout the entire PA range of this camera, and later was more easily detectable in the northern (upper) region. A faint structure was apparent in the southern region, but this appeared to catch up with the earlier "limb" event and the two became indistinguishable. For the purposes of the TH Model we regard this interaction as a region of missing data, that is a region that may contain ICME structure but we were unable to measure it. As with the HI-2A event there were two features observed at larger elongations which became convex-inward towards the edge of the camera. Unlike in HI-2A, the ICME faded from view before it reached the edge of the camera, at around 16:09 UT on 20 November. We believe this is due to the impact of the ICME with STEREO-B.

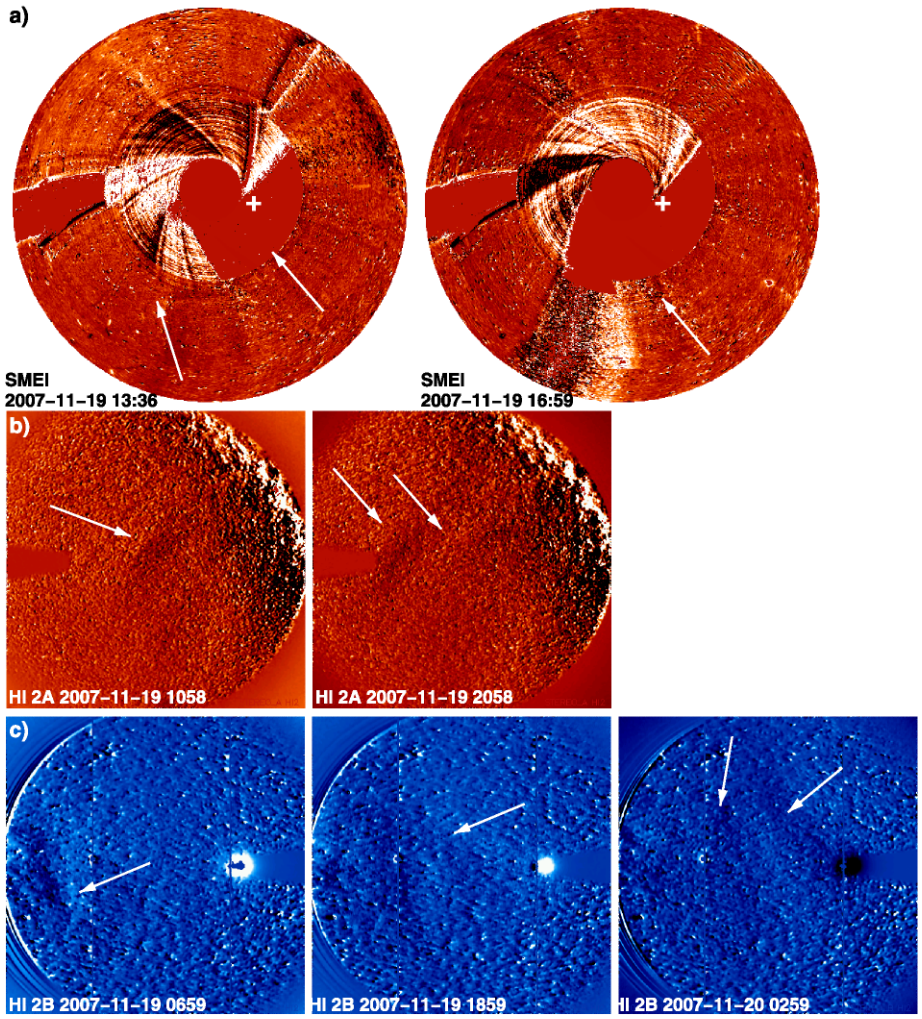

Fig. 2 SMEI and HI-2 images of the ICME counterpart of the November event. (**a**) The zenithal-equidistant ("fisheye") images from SMEI, obtained from 13:36–15:18 and 16:59–18:40 UT on 19 November. The location of the Sun is given by the "+" symbol. (**b**) HI-2A images at 10:58 UT and 20:58 UT on 19 November. The noisy region in the *upper right* of the HI-2A images are residuals from the galactic plane. (**c**) HI-2B images at 06:59 and 18:59 UT on 19 November, and 02:59 UT on 20 November. For HI-2B the *white circles* towards the *right of the left and centre images*, and the *black circle* in the same area in the *right image* are the Earth. The *arrows* indicate the location of the ICME(s) and the instrument and times are labelled on each

3.3 *In Situ* Observations

When it reached distances near 1 AU the ICME passed the STEREO spacecraft themselves, allowing direct measurements using their *in situ* instruments. Near the Earth at the L1 Lagrange point, the ICME was also detected by the ACE spacecraft. Figure 3 shows the magnetometer and plasma data from each of the three spacecraft. Note that we measure the arrival of the ICME by the forward shock signature in each instrument, i.e. the simultaneous jump in B field, density and bulk speed (e.g. Howard and Tappin 2005). This signature is clearly

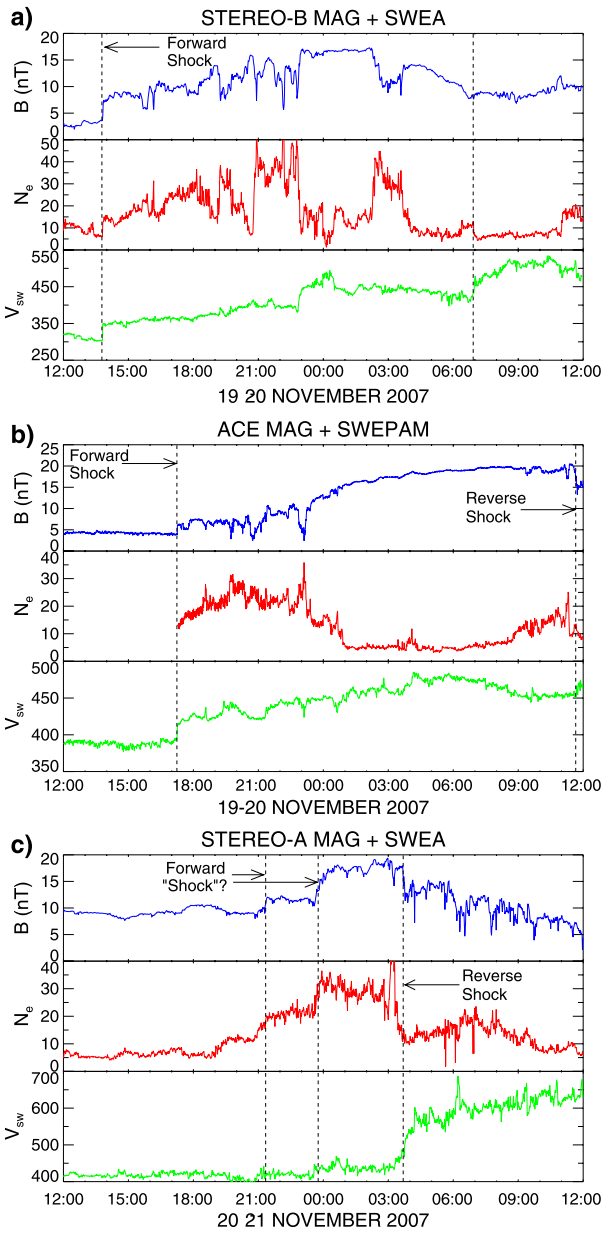

Fig. 3 Magnetic field (*top*), solar wind density (*middle*) and solar wind bulk speed (*bottom*) measurements from the *in situ* instruments aboard (**a**) STEREO-B, (**b**) ACE and (**c**) STEREO-A. The time range for each plot is 19–20 November 2007 (12–12 UT) for panels (**a**) and (**b**), and 20–21 November 2007 (12–12 UT) for panel (**c**). The estimated duration of the ICME is shown in each case

visible in STEREO-B and ACE and are shown in Figs. 3a and 3b. With this signature we can deduce that the ICME arrives first at STEREO-B on 19 November around 13:50 UT then at ACE around 17:15 on the same day. Note that STEREO-B is around 0.04 AU further from the Sun than ACE, so this timing is opposite to what may be expected for an ICME with a spherical shell structure. This is discussed later.

The arrival of the ICME at STEREO-A is somewhat more complicated, as shown in the bottom panels of Fig. 3c. There are no clear forward shock signatures, rather two increases

in B field around 21:30 and 23:45 UT on 20 November. These are accompanied by increases in density and solar wind speed, but at a more gradual rate than is expected for a forward shock. Later, at around 03:30 UT on 21 November there is a relatively strong reverse shock signature (a decrease in B-field and density but an increase in solar wind speed). A much weaker reverse shock also appears in ACE around 12:00 UT on 20 November, and while there is no reverse shock apparent in STEREO-B, we believe the ICME signature ceases around 07:00 UT on 20 November. Thus, the ICME duration is 17 hours 10 minutes in STEREO-B, 18 hours 45 minutes in ACE and only either 4 or 6 hours in STEREO-A. The clear difference in structure between ACE and STEREO-A implies that a different component is observed, suggesting a possible discovery of a new combined structure. This is also discussed later.

3.4 Associated Activity

Other information on this event may be obtained by investigating associated activity. This includes solar "surface" associations and the response of the Earth's magnetic field upon the arrival of the ICME. Figure 4a shows an EIT image around the time of the CME onset (14:00 UT on 15 November). There was a small region of activity in the western hemisphere just south of the equator (indicated by the circle in Fig. 4a). This was not a flare or erupting prominence, but appeared to be a slight brightening and reorganisation of the magnetic structure near this region. While not significant by solar eruptive standards at this wavelength, it was the only activity present on the solar surface during this day. Investigation of X-ray and Hα data (not shown) also reveal no significant activity on this day. In soft X-rays the flux did not exceed 10^{-8} W m^{-2} (i.e. below the A class flare level) all day.

Also indicated in Fig. 4a is a coronal hole to the northeast and southwest of the region of activity. Despite the already-existing presence of a long-duration coronal hole in the vicinity of the region of activity, a smaller new coronal hole opened near the solar equator at around the onset time of the CME. Coronal holes are generally regarded as sources of high-speed solar wind material (e.g. Krieger et al. 1973) and as such are good candidates for the source of corotating interaction regions further from the Sun. Corotating interaction regions, or CIRs (Smith and Wolfe 1976) occur when fast solar wind, typically from coronal holes, interacts with slow solar wind due to corotation at low latitudes, causing a region of compression. CIRs have been investigated for many years, some examples including Pizzo (1978, 1980, 1982), and Tappin et al. (1984). It is possible that some CIR activity may be present during this event. We believe the smaller, newly created coronal hole plays a major role in the overall structure of this event. This is discussed further in later sections.

Given the low speed, absence of flare association and low intensity nature of this CME, one would not expect this event to be geoeffective. Indeed, no space weather alert was issued by the authorities at NOAA (http://www.swpc.noaa.gov/alerts/archive/alerts_Nov2007.html) between 4–19 November (until the Sudden Impulse was detected late on the 19th). Nonetheless, when this event arrived at the Earth, it was the cause of significant geomagnetic activity. Figures 4b and 4c show plots of the K_p and Dst indices for 19–21 November. These indicate that a sudden storm commencement occurred at 18:11 UT on 19 November followed by a geomagnetic storm reaching a maximum K_p of 5+ and minimum Dst of -71 on 20 November.

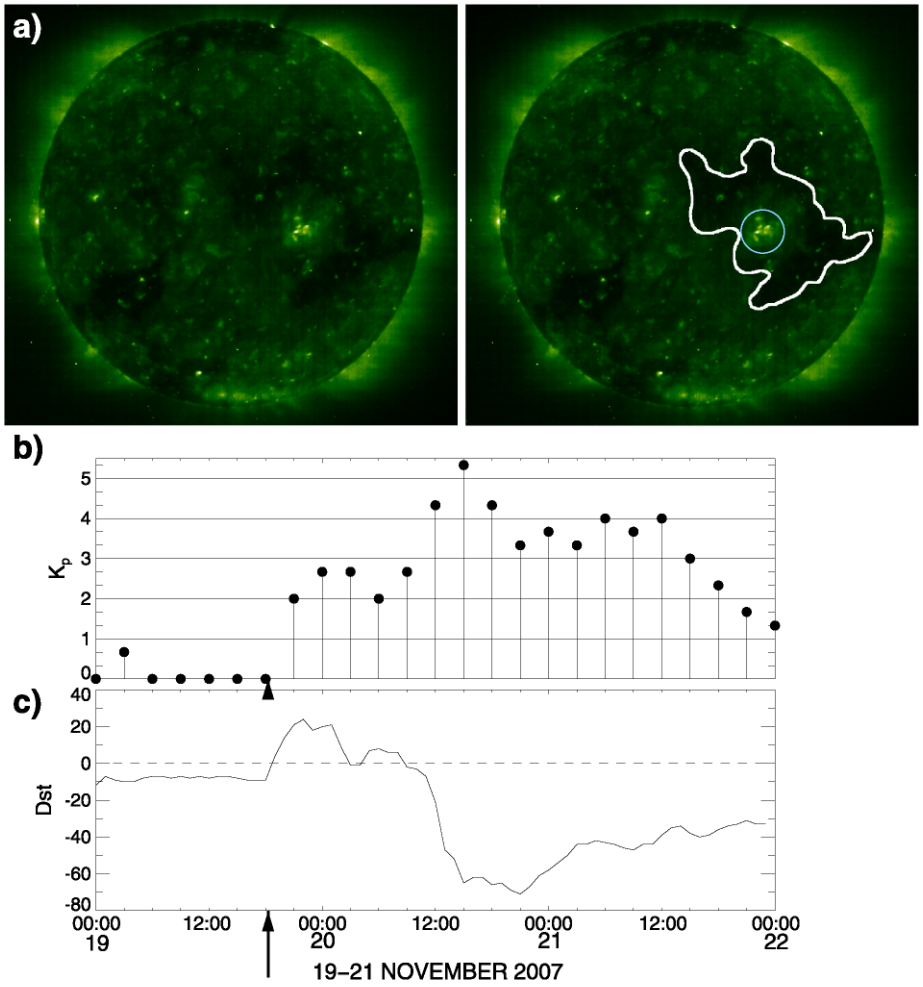

Fig. 4 (**a**) (*Left*) EIT 195 Å image obtained on 14:00 UT on 15 November. (*Right*) The same image with regions of interest indicated. The area enclosed by the *circle* indicates the location of the region where a small amount of activity occurred around the onset time of this CME and the area enclosed by the *white border* indicates a coronal hole. (**b**) Plot of K_p index against time on 19–21 November. (**c**) Plot of Dst index against time on 19–21 November. Regions of high K_p and low Dst indicate the occurrence of a geomagnetic storm. The time of the related sudden storm commencement at 18:11 on 19 November is indicated by the *arrow* (*arrowhead*) in both plots

4 Reconstructing the 3-D ICME

4.1 The TH Model

To reconstruct the 3-D structure of this ICME, we use the SMEI, HI-1B and HI-2 images and apply what has become known as the TH Model. This model compares leading edge measurements from heliospheric images with apparent leading edges from simulated ICMEs and determines the optimum parameters describing the observed ICME. These leading edges are based on measurements from the ICME observed in heliospheric images (SMEI and

HI) only, and do not use measurements from coronagraphs or other instruments. This is achieved by comparing a data cube containing over 300 000 simulated ICME images with a sequence of leading edge measurements. The simulated leading edges are constructed using unique combinations of parameters describing the ICME structure, direction of propagation and 3-D kinematic properties. The result is a 3-D reconstruction of the ICME from the parameters describing its structure and kinematic evolution. It was constructed using the theory described in Paper 1 and its development and usage are discussed in Paper 2. Paper 2 describes the utility of this model applied to two events observed by SMEI in 2004.

4.2 Modification of the TH Model

To accommodate for the different viewpoints of STEREO, it was necessary to make some extensions to the TH Model. This was because of the relative radial and longitude locations of each spacecraft.

The different radial distances of the two STEREO spacecraft are sufficient to alter the perspective, and significantly different results are obtained if it is ignored (this was tested, but the results are not shown here). To account for this we generated new databases of edge locations calculated for observers at 0.95 and 1.05 AU from the Sun as well as the existing databases at 1.0 AU. This is one grid point in the Model, and corresponds approximately to the heliocentric distances of STEREO-A and STEREO-B respectively. The actual distances of STEREO-A, B and Earth at the time of the event were 0.97, 1.04 and 0.99 AU.

Since all three spacecraft are close to the ecliptic plane, and our grid is heliocentric ecliptic, the longitude differences can be addressed by a simple shift of the central longitude of the ICME.

Because it is necessary to include the complete ICME position angle coverage in order to run the TH Model, the HI data alone did not provide adequate coverage of this event. Nor in this case could the SMEI data alone, as it had large sections of the sky obscured by noise. So it was necessary to combine the three instruments HI-A, HI-B and SMEI.

Thus the fitting is handled by taking all the data together and tagging each measurement with the identity of the spacecraft making it. Then when we determine the mismatch of each point, we can use the appropriate edge database for the spacecraft, and shift the central longitude of the simulated ICME by the appropriate amount before calculating its edge.

For the Stage 2 fitting, we have the option of fitting all the spacecraft simultaneously, or of selecting one spacecraft.

5 Results

Table 1 shows the Stage 1 converging parameters for the ICME using 10 runs in the same manner as for Paper 2. To summarise, the best fitting ICME was a spherical shell of central location 3°N 17°E, latitude width of 74° and longitude width of 94°. Hence, the central axis is closest to the physical location of STEREO-B and the ICME easily passes through the Earth and STEREO-B, and grazes STEREO-A.

Contour plots showing the constraints of the parameters are shown in Fig. 5. The layout for these is identical to those in Paper 2. It is immediately clear that unlike the corresponding plots in Paper 2, we do not see the abrupt discontinuities in the mismatch parameter. We believe this is because the slope changes that occur at the grid points in the database do not occur at the same places for the different viewpoints, and as a result these effects are smeared out.

Table 1 Stage 1 fitting results for the ICME. The bold row is the "best" fit, the parameters of which were used to feed Stage 2. The average (Avg) and standard deviation (σ) of the 10 runs are also shown. The starting heights were determined at 04:28 on 17 November 2007

Run #	Start height (AU)	Average speed (km s^{-1})	Central latitude (°)	Central longitude (°)	Longitude size (°)	Latitude size (°)	Mismatch (°)
0	0.36	458.08	0.00	−12.00	34.20	28.11	3.43
1	0.34	474.16	10.08	−17.28	44.76	53.53	3.46
2	**0.34**	**469.47**	**3.06**	**−18.00**	**43.87**	**36.00**	**3.42**
3	0.33	477.57	1.91	−12.00	42.11	35.83	3.43
4	0.33	478.35	1.49	−24.00	55.52	37.08	3.42
5	0.33	484.23	3.52	−5.16	38.55	35.58	3.45
6	0.36	458.26	0.01	−29.94	52.66	31.60	3.42
7	0.36	460.24	0.06	−24.00	47.99	30.51	3.42
8	0.31	501.76	12.06	−2.44	60.00	47.47	3.45
9	0.34	475.06	1.90	−24.96	55.17	36,00	3.42
Avg	0.34	473.72	3.41	−16.98	47.48	37.17	
σ	0.02	13.41	4.24	9.02	8.25	7.73	

It is also evident that the minima are very shallow, compared with those we obtained in Paper 2. This is most likely because the simple geometrical shapes we use do not perfectly fit the real structure, and as a result the best parameters for each spacecraft are somewhat different, thus spreading the minimum. It should however be noted that when we attempted to fit the spacecraft individually, the results were wildly unstable. This is almost certainly because in this case we had rather limited coverage in position angle in all 3 spacecraft (not even SMEI had 180° of usable coverage) and so with no defined position angle edges to the structure, anything from the size of the observable region to a full halo could be fitted.

Figure 6 shows the kinematic properties of the ICME derived from the Stage 2 fitting of the TH Model. Three plots are shown, the 3-D heliospheric distance in AU, speed, and the distance plot with associated CME height-time and *in situ* data (times of forward shock arrival) overlayed. Two columns of the plots of the same parameters are shown. The first column shows the collective data from all three imagers (SMEI, HI-A and HI-B) while the second shows only the HI-B data, which due to the relatively larger number of measurements by far dominated the outcome of the Model convergence. With the exception of a small number of early data points (obtained from the HI-1A measurements), it appears the ICME accelerates for over a day before it undergoes a sharp deceleration. The rate of acceleration varies depending on the selected data set (either from 300–1000 or 300–600 km s^{-1}) but a clear sudden change to its acceleration occurs just before noon on 19 November, four days after launch and when the ICME is near 0.9 AU. This may or may not be physical, and required an additional survey of numerous events, beyond the scope of the present study.

For comparison with external data from which the Model was not derived (including coronagraph data), Fig. 6c shows the same 3-D data from Fig. 6a, but extended to allow for the inclusion of both the associated CME height-time data and the times of the shock arrival at each spacecraft. In order to improve clarity, Fig. 7 shows the regions of the plots where confusion from overlap from the three spacecraft dominates. Figure 7a shows the latter section of the heliospheric image data, while Fig. 7b shows the coronagraph height-

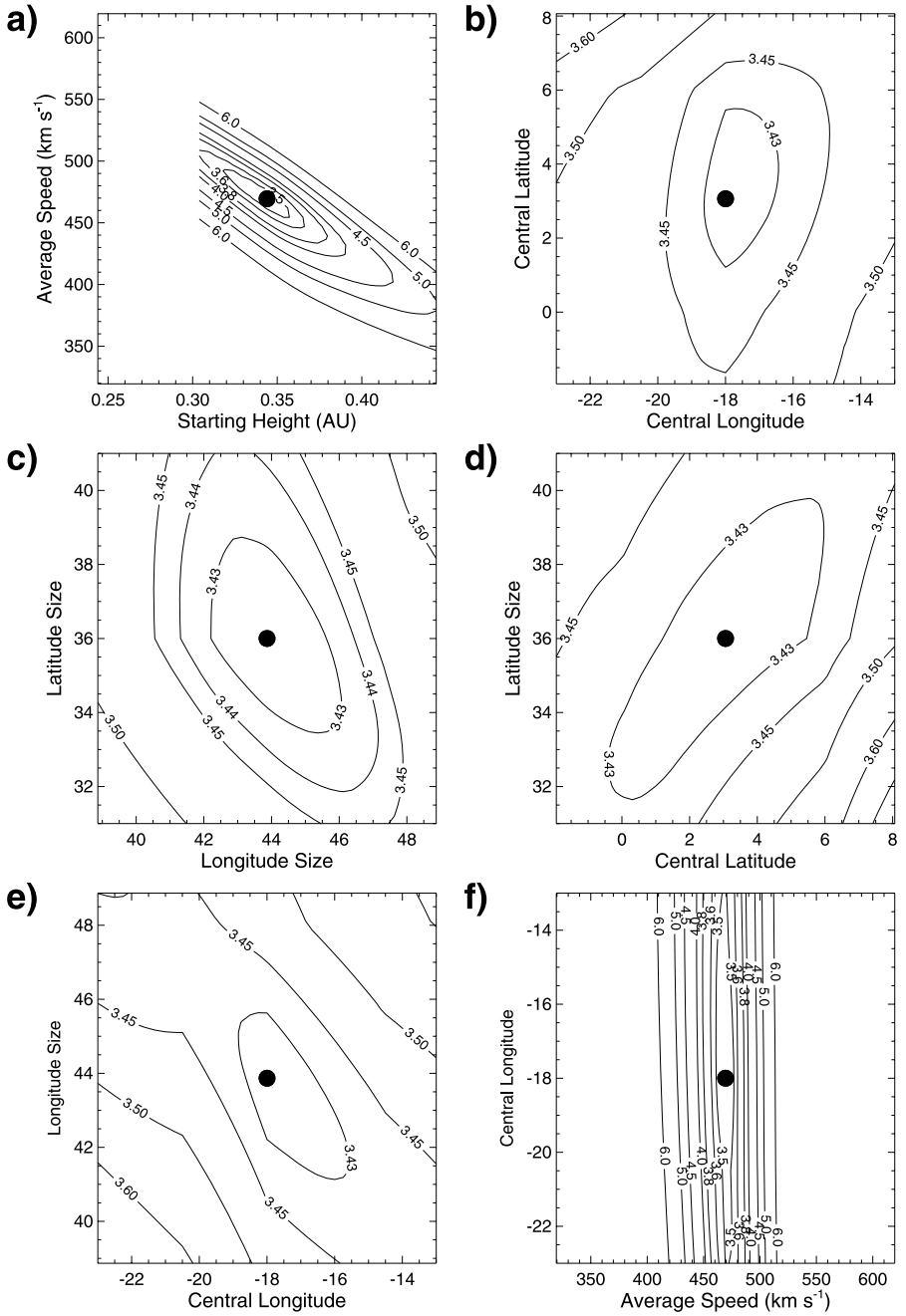

Fig. 5 A demonstration of how well each parameter is constrained for the Stage 1 convergence: error contours of selected parameter combinations. (**a**) Average speed vs starting height, (**b**) central latitude vs central longitude, (**c**) latitude size vs longitude size, (**d**) latitude size vs central latitude, (**e**) longitude size vs central longitude and (**f**) central longitude vs average speed. In each case the actual converged parameter is indicated by the *filled circle*. Contour values represent the mismatch parameter described in Paper 2

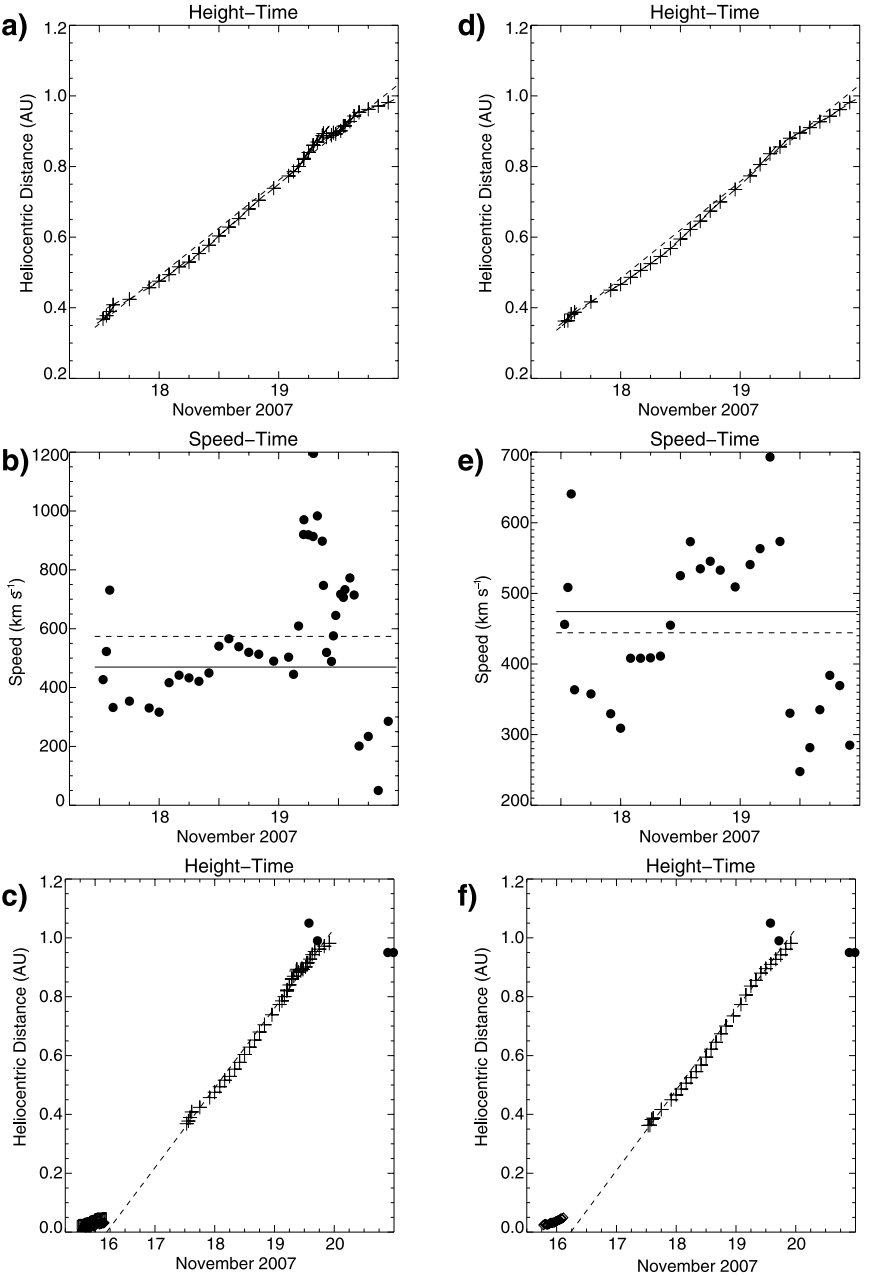

Fig. 6 Kinematic plots against time for the parameters derived from the Stage 2 processing of the Model. The *left column* shows the results from all three spacecraft while the *right column* shows only results from HI-B, measurements from which dominated the convergence of the model. (**a**) Modelled 3-D heliocentric distance for the heliospheric images alone, plotted as a function of time. (**b**) Derived speed at each point vs time. The *solid horizontal line* indicates the Stage 1 fit, and the *dashed line* is the average of the Stage 2 fits. (**c**) The same heliospheric image results from (**a**) extended to the full range from 0–1.2 AU. This allows (and includes) height-time data from the coronagraphs for the associated CME as well as the times and locations of the shocks at each spacecraft

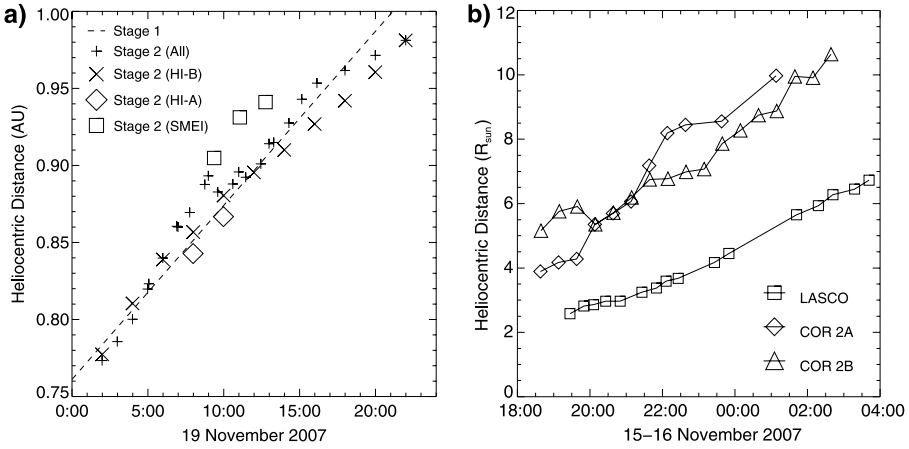

Fig. 7 Close-up views of the sections of Fig. 6c (*left*) which are difficult to view due to multiple spacecraft measurements. (**a**) Distance-time plot of the latter part of the ICME evolution including data from each individual instrument. The linear plot for the constant speed Stage 1 fit. (**b**) Coronagraph height-time data showing plots from each spacecraft. Distances here are given in solar radii (1 AU ∼215 $R_{\odot}$)

time plots. The coronagraph data show an acceleration early in the evolution of the CME, which we believe continues to large distances from the Sun. The SMEI data appear to be at larger distances than those from both STEREOs at the same times. We believe this may be because of the smearing of the edges of the structure caused by the long exposure in the STEREOs. This may have caused us to mark the leading edge lower in the structure that we did with the sharper edges in SMEI. This long exposure effect of ICMEs observed in the HIs is significant, and one we believe to be a drawback in the design of the HI-2 instrument.

6 Discussion

6.1 Structure

Figure 8 shows the 3-D reconstruction from the Model from three perspectives. Figure 8a shows a selected SMEI image (the same as from Fig. 2a) with the measured ICME leading edge and ε-PA grid superimposed. The projected image of the modelled ICME is shown in Fig. 8b with its leading edge at 0.91 AU shown. Finally, the actual 3-D reconstruction from the perspective of the Ulysses spacecraft (to remain consistent with similar plots in Paper 2) is shown in Fig. 8c. Here, the ICME structure is at 0.9 AU and the locations of the Earth (and SMEI), STEREO-A and STEREO-B are shown. The Model shows the ICME easily impacts the Earth and STEREO-B and just grazes STEREO-A. Using the Stage 1 constant speed assumption we predict the arrival time of this ICME at STEREO-B, ACE and STEREO-A is 01:36 UT on 20 November, and 20:13 and 18:12 UT on 19 November, respectively. As noted in Sect. 3.3 the shock arrival times at each spacecraft are 13:50 and 17:15 UT on 19 November, and 21:30 or 23:45 UT on 20 November respectively. As with the results in Stage 2, the model performs well in predicting the arrival time at ACE (3 hours, 28 minutes early), but its prediction is less accurate for STEREO-B and significantly different for STEREO-A.

In order to accurately describe the structure of this event, it is necessary to describe the appearance of the event in all of the instruments that have been used in its observation. While

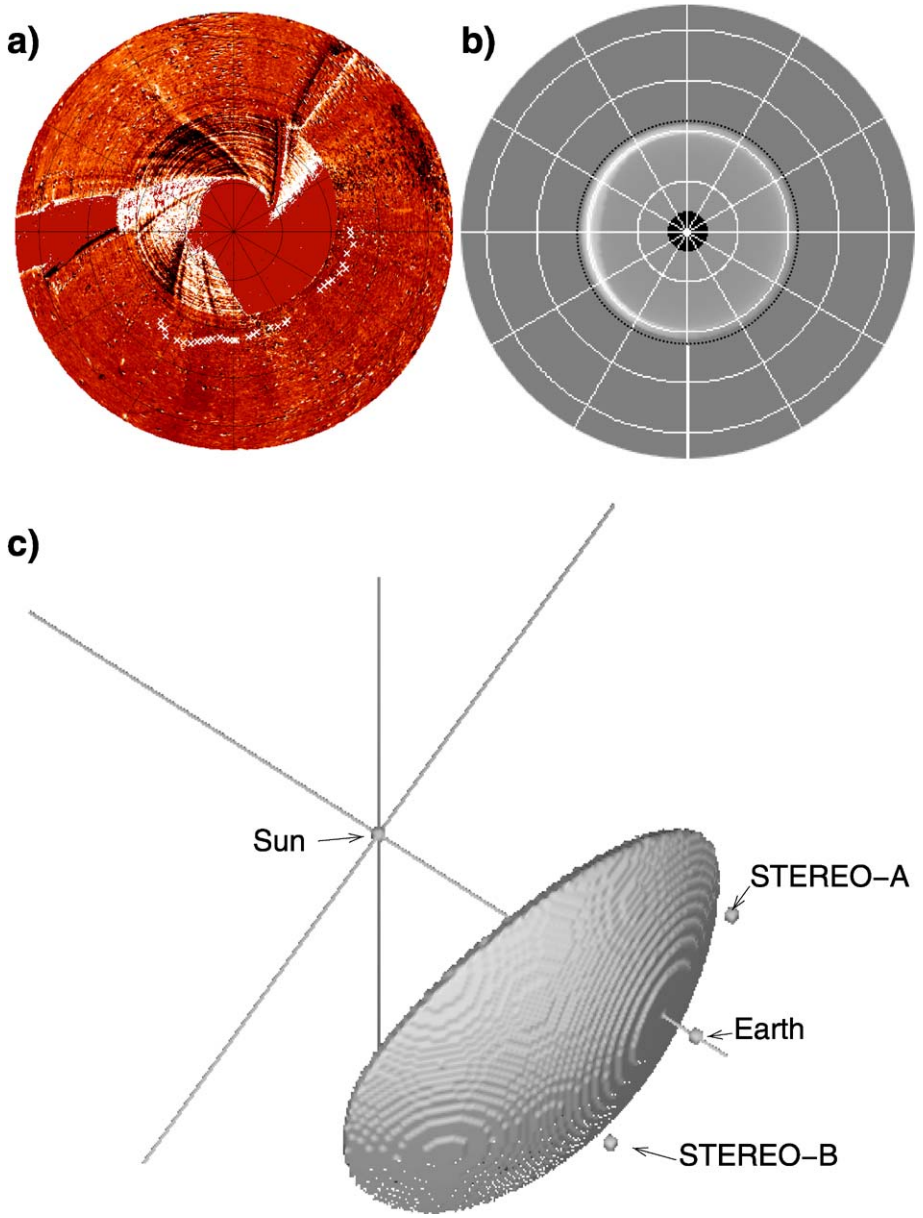

Fig. 8 The three-dimensional reconstruction of the ICME as determined by the TH Model convergence. (**a**) SMEI "fisheye" image on 19 November (13:36–15:18 UT) with the measured leading edge and ε-PA grid superimposed. (**b**) The modelled leading edge at 14:00 UT (0.91 AU) overlayed on a "fisheye" projection of the modelled ICME at a distance of 0.9 AU. (**c**) The 3-D reconstruction of the modelled ICME at a distance of 0.91 AU. The location of the Earth (and SMEI), STEREO-A and STEREO-B are shown. As with the same plot in Paper 2, we have chosen to show the appearance from the direction of the Ulysses spacecraft, which was 57°N and 56°E (ecliptic coordinates) at the time of this event

a good first-order estimate of the structure may be produced using heliospheric image data alone, we may refine this structure using our knowledge of the passage of the event through each spacecraft.

We first present a summary of the clues from the large variety of datasets associated with this event:

1. The CME component appears as a partial halo by all three spacecraft. A separate, but possibly related component appears to the east of LASCO and STEREO-A (predominantly the latter), but only the single westward component is observed by STEREO-B.
2. To the west of the active region associated with the CME launch is a low-latitude coronal hole. This appears to be enlarged or a new coronal hole is created to the south of the active region following the launch of the CME.
3. 3-D reconstruction using the heliospheric images and the TH Model results in a central axis at 17°E, i.e. with its centre much closer to STEREO-B than the Earth.
4. The *in situ* data appear very similar in STEREO-B and ACE (led by a strong forward shock, followed by a weak reverse shock and lasting around 18 hours) but very different in STEREO-A (weak, if any, forward shock, strong reverse shock and only 5 hours in duration). Furthermore the *in situ* event observed in STEREO-A appears very much like a "classical" corotating interaction region signature (e.g. Smith and Wolfe 1976; Burlaga 1995), while the signature in STEREO-B and ACE resemble a standard ICME much more closely.
5. The ICME impacted STEREO-B first, then ACE $3\frac{1}{2}$ hours later, but it did not arrive at STEREO-A until 28 hours after its impact with ACE.
6. The associated geomagnetic storm, caused by the arrival of this event at the Earth, began around 18:00 UT on 19 November and hence was well underway when the ICME arrived at STEREO-A (which is closer to the Sun than the Earth is) towards the end of 20 November.

This combination of evidence leads us to the firm conclusion that this event is a combination two structures:

1. A fairly typical CME/ICME which passes STEREO-B and ACE;
2. A CIR structure which passes STEREO-A.

The merger between these two structures occurs somewhere between the Earth and STEREO-A, probably closer to STEREO-A. This means the Modelled longitude extent would be shortened at its western flank. Also, the CME/ICME component can be made to intercept STEREO-B before the Earth if we allow the curvature of the shell to be slightly greater than the sphere assumed by the TH Model.

Figure 9 shows two ecliptic slices of the likely structure of this event, around the time of impact with (a) STEREO-B and ACE on 19 November and (b) STEREO-A on 20 November. Note that the distortion of the spherical shell structure need not be large for the event to pass STEREO-B before passing the Earth (for comparison, Modelled ecliptic slice of the spherical shell is included). This is because the central longitude of the ICME structure is much closer to STEREO-B. Also note that when the CIR component arrives at STEREO-A, the CME component has long passed the Earth and STEREO-B. This is indicated by the onset time of the geomagnetic storm shown in Fig. 4 and explains the large time difference between the arrival of the event at ACE and at STEREO-A.

Physically, it is likely the CIR component is the result of a fast-flowing column of solar wind material brought about by the creation of a new smaller coronal hole by the launch of the original CME. In much the same way as many CMEs move through a region of slower

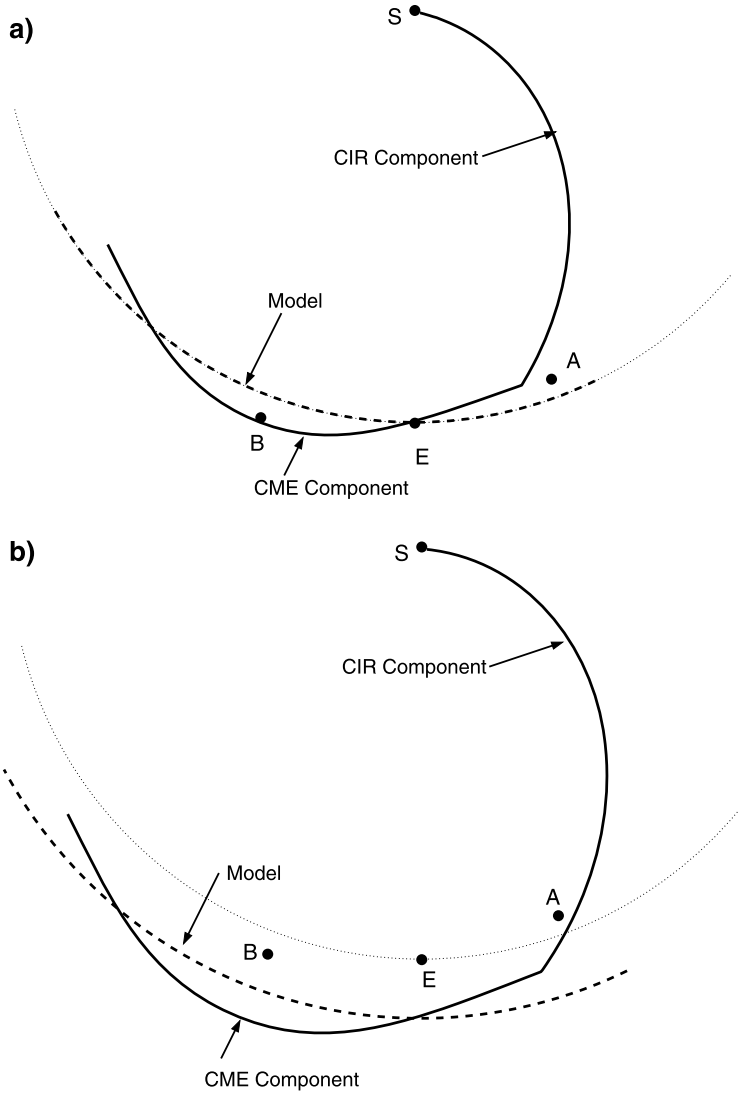

Fig. 9 Ecliptic plane projection (looking from the north) of the 3-D reconstruction of the event in the present study, along with the locations of the Earth (E) and both STEREO spacecraft (A and B). This comprises of a CME component that passes STEREO-B and the Earth and a CIR component to the west that intersects STEREO-A. This event is shown at two times: (**a**) When the event was near STEREO-B and the Earth on 19 November; and (**b**) when the event was near STEREO-A towards the end 20 November. The results of the TH Model at each time is shown as the *dashed arc* and the *dotted arc* represent the orbit of the Earth

solar wind, so too will this fast-flowing column, which corotates with the Sun and creates the commonly-recognised CIR structure. Hence the overall ICME structure is a combination of the two. With the exception of a mention of this possibility (Tappin 1984; Hewish et al. 1985), we believe that this is the first time sufficient evidence to support the existence of such a structure has appeared in the literature.

6.2 Kinematic Evolution

Assuming the Stage 2 results apply to the CME component only (the likely evolution and nature of the CIR component is well documented) we may also discuss the kinematic evolution of this event. Figure 6 shows what appears to be a three-part evolution for this ICME. Early in the evolution the speed appears to be much higher than in the coronagraphs. This is followed by a period of deceleration followed by a gradual acceleration until around 12:00 UT on 19 November, and then a sudden deceleration follows. The first high speed component may be questionable as it is derived from the HI-1 measurements in a regime where the geometry in Paper 1 is less certain. The sudden deceleration may be physically questionable as well, and further study is required on a large number of events to resolve this. Whether these components are regarded or not, it is clear that there is a sustained acceleration that continues until the CME is at a distance of around 0.9 AU from the Sun. It is unclear whether the acceleration is a continuation of or secondary to the initial acceleration observed in the coronagraphs, but the transition between the acceleration and deceleration regimes is relatively sudden, if it turns out to be physical.

This long-duration acceleration has been identified in interplanetary scintillation ICME observations by Manoharan et al. (2001) and Manoharan (2006) and in SMEI data by Tappin (2006) and Howard et al. (2007). Such an acceleration was also apparent in the first event of Paper 2. Physically its source has been suggested as one of two likely possibilities by Howard et al. (2007):

1. A Lorentz force, brought about by the interaction between the internal toroidal current within the CME and the surrounding poloidal interplanetary magnetic field;
2. Internal pressure by the fast solar wind flowing from the coronal hole produced by the slower CME.

The former has been modelled to large distances by Chen (1996) and is the generally accepted description for this driving force (e.g. Vršnak 1990, 1992 and references therein). The distance beyond which the Lorentz force becomes insignificant, however, is believed to be much closer to the Sun than that for the present event.

The latter is described as a fast flowing plasma in the wake of the CME exerting a force on the slower moving CME shock front (Steinitz and Eyni 1980; Hewish et al. 1985). The result is a necessary increase in the overall speed of the CME as required by the conservation of momentum flux. As the present event originated from the Sun with a relatively low speed, the ambient flow of the solar wind is likely to also contribute to an increase in solar wind. Additionally, the connected CIR structure lends evidence to support the creation of a fast flowing stream in the wake of the CME eruption.

7 Conclusions

The purposes of the present study are fourfold:

1. To demonstrate the versatility of the TH Model by its accommodation of STEREO HI data;
2. To improve the accuracy of the Model by applying it to an event which required all three spacecraft combined to produce sufficient 3-D information (each imager alone was insufficient for such a reconstruction);

3. To combine the heliospheric image results with external associated data (*in situ*, surface associations, coronagraph counterparts) to produce an accurate 3-D reconstruction of the ICME for the first time;
4. To present evidence of a new class of ICME; that of a combination of a "standard" with a CIR structure extending from its western flank.

Physically, the ICME structure we have suggested lends evidence to the possibility that this ICME may be driven by a column of fast-flowing solar wind in its wake, brought about by the launch of the initial CME itself. We believe that this structure is quite common among (particularly initially slow) CMEs and that this may be an alternative driving force to the commonly accepted Lorentz force. It is not until now that sufficient details can be extracted from the combination of image and *in situ* data from a variety of sources that such a reconstruction was possible.

It was found that the ICME component of the structure could be more accurately depicted if we allowed a small increase in curvature beyond the simple spherical shell allowed for by the Model. It seems clear that the Model could be made more accurate if it could accommodate such distortions to the curvature of the shell. We are in the process of modifying the Model for just such an accommodation, removing the need for a distorted bubble, and instead introducing a distortion factor to the shell alone. Results from the next version of the TH Model will be presented in a later report.

Acknowledgements This work is supported in part by the National Research Council Fellowship Program, funded by AFOSR contract F49620-02C-0015. The National Solar Observatory is operated by AURA, Inc., under cooperative agreement with the National Science Foundation. Partial support for NSO is provided by the USAF under a Memorandum of Agreement.

References

M.H. Acuña, D. Curtis, J.L. Scheifele, C.T. Russell, P. Schroeder, A. Szabo, J.G. Luhmann, Space Sci. Rev. **136**, 203–226 (2008)

G.E. Brueckner, R.A. Howard, M.J. Koomen, C.M. Korendyke, D.J. Michels, J.D. Moses, D.G. Socker, K.P. Dere, P.L. Lamy, A. Llebaria, M.V. Bout, R. Schwenn, G.M. Simnett, D.K. Bedford, C.J. Eyles, Solar Phys. **162**, 357–402 (1995)

L.F. Burlaga, *Interplanetary Magnetohydrodynamics* (Oxford University Press, New York, 1995)

P.J. Cargill, Solar Phys. **221**, 135–149 (2004)

J. Chen, J. Geophys. Res. **101**, 27499–27519 (1996)

A. Dal Lago, L.E.A. Viera, E. Echer, W.D. Gonzalez, A.L.C. De Gonzalez, F.L. Guarnier, N.J. Schuch, R. Schwenn, Solar Phys. **222**, 323–328 (2004)

J.-P. Delaboudinière, G.E. Artzner, J. Brunaud, A.H. Gabriel, J.F. Hochedez, F. Millier, X.Y. Song, B. Au, P. Dere, R.A. Howard, R. Kreplin, D.J. Michels, J.D. Moses, J.M. Defise, C. Jamar, P. Rochus, J.P. Chauvineau, J.P. Marioge, R.C. Catura, J.R. Lemen, L. Shing, R.A. Stern, J.B. Gurman, W.M. Neupert, A. Maucherat, F. Clette, P. Cugon, E.L. Van Dessel, Solar Phys. **162**, 291–312 (1995)

C.J. Eyles, R.A. Harrison, C.J. Davis, N.R. Waltham, B.M. Shaughnessy, H.C.A. Mapson-Menard, D. Bewsher, S.R. Crothers, J.A. Davies, G.M. Simnett, R.A. Howard, J.-P. Halain, J.-M. Defise, E. Mazy, P. Rochus, Solar Phys. **254**, 387–445 (2009)

C.J. Eyles, G.M. Simnett, M.P. Cooke, B.V. Jackson, A. Buffington, N.R. Waltham, J.M. King, P.A. Anderson, P.E. Holladay, Solar Phys. **217**, 319–347 (2003)

C.D. Fry, W. Sun, C.S. Deehr, M. Dryer, Z. Smith, S.-I. Akasofu, M. Tokumaru, M. Kojima, J. Geophys. Res. **106**, 20985–21002 (2001)

A.B. Galvin, L.M. Kistler, M.A. Popecki, C.J. Farrugia, K.D.C. Simunac, L. Ellis, E. Möbius, M.A. Lee, M. Boehm, J. Carroll, A. Crawshaw, M. Conti, P. Demaine, S. Ellis, J.A. Gaidos, J. Googins, M. Granoff, A. Gustafson, D. Heirtzler, B. King, U. Knauss, J. Levasseur, S. Longworth, K. Singer, S. Turco, P. Vachon, M. Vosbury, M. Widholm, L.M. Blush, R. Karrer, P. Bochsler, H. Daoudi, A. Etter, J. Fischer, J. Jost, A. Opitz, M. Sigrist, P. Wurz, B. Klecker, M. Ertl, E. Seidenschwang, R.F. Wimmer-Schweingruber, M. Koeten, B. Thompson, D. Steinfeld, Space Sci. Rev. **136**, 437–486 (2008)

H. Hakamada, S.-I. Akasofu, Space Sci. Rev. **31**, 3–70 (1982)
R.A. Harrison, C.J. Davis, C.J. Eyles, D. Bewsher, S.R. Crothers, J.A. Davies, R.A. Howard, D.J. Moses, D.G. Socker, J.S. Newmark, J.-P. Halain, J.-M. Defise, E. Mazy, P. Rochus, D.F. Webb, G.M. Simnett, Solar Phys. **247**, 171–193 (2008)
A. Hewish, S.J. Tappin, G.R. Gapper, Nature **314**, 137–140 (1985)
R.A. Howard, J.D. Moses, A. Vourlidas, J.S. Newmark, D.G. Socker, S.P. Plunkett, C.M. Korendyke, J.W. Cook, A. Hurley, J.M. Davila, W.T. Thompson, O.C. St. Cyr, E. Mentzell, K. Mehalick, J.R. Lemen, J.P. Wuelser, D.W. Duncan, T.D. Tarbell, C.J. Wolfson, A. Moore, R.A. Harrison, N.R. Waltham, J. Lang, C.J. Davis, C.J. Eyles, H. Mapson-Menard, G.M. Simnett, J.P. Halain, J.M. Defise, E. Mazy, P. Rochus, R. Mercier, M.F. Ravet, F. Delmotte, F. Auchere, J.-P. Delaboudinière, V. Bothmer, W. Deutsch, D. Wang, N. Rich, S. Cooper, V. Stephens, G. Maahs, R. Baugh, D. Mcmullin, Space Sci. Rev. **136**, 67–115 (2008a)
T.A. Howard, C.D. Fry, J.C. Johnston, D.F. Webb, Astrophys. J. **667**, 610–625 (2007)
T.A. Howard, D. Nandy, A.C. Koepke, J. Geophys. Res. **113**, A01104 (2008b). doi:10.1029/2007JA012500
T.A. Howard, S.J. Tappin, Astron. Astrophys. **440**, 373–383 (2005)
T.A. Howard, S.J. Tappin, Solar Phys. **252**, 373–383 (2008)
T.A. Howard, S.J. Tappin, Space Sci. Rev. (2009, this issue)
T.A. Howard, D.F. Webb, S.J. Tappin, D.R. Mizuno, J.C. Johnston, J. Geophys. Res. **111**, A04105 (2006). doi:10.1029/2005JA011349
B.V. Jackson, A. Buffington, P.P. Hick, R.C. Altrock, S. Figueroa, P.E. Holladay, J.C. Johnston, S.W. Kahler, J.B. Mozer, S. Price, R.R. Radick, R. Sagalyn, D. Sinclair, G.M. Simnett, C.J. Eyles, M.P. Cooke, S.J. Tappin, T. Kuchar, D.R. Mizuno, D.F. Webb, P.A. Anderson, S.L. Keil, R.E. Gold, N.R. Waltham, Solar Phys. **225**, 177–207 (2004)
M.L. Kaiser, T.A. Kucera, J.M. Davila, O.C. St. Cyr, M. Guhathakurta, E. Christian, Space Sci. Rev. **136**, 5–16 (2008)
A.S. Krieger, A.F. Timothy, E.C. Roelof, Solar Phys. **29**, 505–525 (1973)
R.P. Lepping, J.A. Jones, L.F. Burlaga, J. Geophys. Res. **95**, 11957–11965 (1990)
B.J. Lynch, T.H. Zurbuchen, L.A. Fisk, J. Geophys. Res. **108**, 1239–1252 (2003)
P.K. Manoharan, Solar Phys. **235**, 345–368 (2006)
P.K. Manoharan, M. Tokumaru, M. Pick, P. Subramanian, F.M. Ipavich, K. Schenk, M.L. Kaiser, R.P. Lepping, A. Vourlidas, Astrophys. J. **559**, 1180–1189 (2001)
K. Marubashi, S. Sung, S. Bong, K. Cho, EOS Trans. AGU, **89**, Fall Meet. Suppl., SH13B-1557 (2008)
C. Möstl, C.J. Farrugia, C. Miklenic, M. Temmer, A.B. Galvin, J.G. Luhmann, H.K. Biernat, K.E. Huttunen, M. Leitner, T. Nieves-Chinchilla, A. Veronig, EOS Trans. AGU, **89**, Fall Meet. Suppl., SH23B-1634 (2008)
D.J. McComas, S.J. Blame, P. Barker, W.C. Feldman, J.L. Phillips, P. Riley, J.W. Griffee, Space Sci. Rev. **86**, 563–612 (1998)
M. Mierla, J. Davila, W. Thompson, B. Inhester, N. Srivastava, M. Kramar, O.C. St. Cyr, G. Stenborg, R.A. Howard, Solar Phys. **252**, 385–396 (2008)
V. Pizzo, J. Geophys. Res. **83**, 5563–5572 (1978)
V. Pizzo, J. Geophys. Res. **85**, 727–743 (1980)
V. Pizzo, J. Geophys. Res. **87**, 4374–4394 (1982)
A.A. Reinard, Astrophys. J. **682**, 1289–1305 (2008)
J.-A. Sauvaud, D. Larson, C. Aoustin, D. Curtis, J.-L. Médale, A. Federov, J. Rouzaud, J. Luhmann, T. Moreau, L.P. Schröder, I. Dandouras, E. Penou, Space Sci. Rev. **136**, 227–239 (2008)
C.W. Smith, M.H. Acuña, L.F. Burlaga, J. L'Heureux, N.F. Ness, J. Scheifele, Space Sci. Rev. **86**, 613–632 (1998)
E.J. Smith, J.H. Wolfe, Geophys. Res. Lett. **3**, 137–140 (1976)
O.C. St. Cyr, R.A. Howard, N.R. Sheeley Jr., S.P. Plunkett, D.J. Michels, S.E. Paswaters, M.J. Koomen, G.M. Simnett, B.J. Thompson, J.B. Gurman, R. Schwenn, D.F. Webb, E. Hildner, P.L. Lamy, J. Geophys. Res. **105**, 18169–18185 (2000)
R. Steinitz, M. Eyni, Astrophys. J. **241**, 417–424 (1980)
S.J. Tappin, PhD thesis, Cambridge (1984)
S.J. Tappin, Solar Phys. **233**, 233–248 (2006)
S.J. Tappin, A. Buffington, M.P. Cooke, C.J. Eyles, P.P. Hick, P.E. Holladay, B.V. Jackson, J.C. Johnston, T. Kuchar, D. Mizuno, J.B. Mozer, S. Price, R.R. Radick, G.M. Simnett, D. Sinclair, N.R. Waltham, D.F. Webb, Geophys. Res. Lett. **31**, L02802 (2004). doi:10.1029/2003GL018766
S.J. Tappin, T.A. Howard, Space Sci. Rev. (2009, this issue)
S.J. Tappin, A. Hewish, G.R. Gapper, Planet. Space Sci. **32**, 1273–1281 (1984)
W.T. Thompson, N.L. Reginald, Solar Phys. **250**, 443–454 (2008)
D. Tripathi, V. Bothmer, H. Cremades, Astron. Astrophys. **422**, 337–341 (2004)

B. Vršnak, Solar Phys. **129**, 295–312 (1990)
B. Vršnak, Ann. Geophys. **10**, 344–353 (1992)
D.F. Webb, T.A. Howard, C.D. Fry, T.A. Kuchar, D. Odstrčil, B.V. Jackson, M.M. Bisi, R.A. Harrison, J.S. Morrill, R.A. Howard, J.C. Johnston, Solar Phys. **256**, 239–269 (2009)
D.F. Webb, D.R. Mizuno, A. Buffington, M.P. Cooke, C.J. Eyles, C.D. Fry, L.C. Gentile, P.P. Hick, P.E. Holladay, T.A. Howard, J.G. Hewitt, B.V. Jackson, J.C. Johnston, T.A. Kuchar, J.B. Mozer, S. Price, R.R. Radick, G.M. Simnett, S.J. Tappin, J. Geophys. Res. **111**, A12101 (2006). doi:10.1029/2006JA011655
H. Xie, L. Ofman, G. Lawrence, J. Geophys. Res. **109**, A03109 (2004). doi:10.1029/2003JA010226
S. Yashiro, N. Gopalswamy, G. Michalek, O.C. St. Cyr, S.P. Plunkett, R.A. Howard, J. Geophys. Res. **109**, A07105 (2004). doi:10.1029/2003JA010282